CHEMISTRY

MoS_2 pixel arrays for real-time photoluminescence imaging of redox molecules

M. F. Reynolds[1]*, M. H. D. Guimarães[1,2]*, H. Gao[3,4], K. Kang[3,4], A. J. Cortese[1], D. C. Ralph[1,2], J. Park[2,3,4], P. L. McEuen[1,2†]

Measuring the behavior of redox-active molecules in space and time is crucial for understanding chemical and biological systems and for developing new technologies. Optical schemes are noninvasive and scalable, but usually have a slow response compared to electrical detection methods. Furthermore, many fluorescent molecules for redox detection degrade in brightness over long exposure times. Here, we show that the photoluminescence of "pixel" arrays of monolayer MoS_2 can image spatial and temporal changes in redox molecule concentration. Because of the strong dependence of MoS_2 photoluminescence on doping, changes in the local chemical potential substantially modulate the photoluminescence of MoS_2, with a sensitivity of 0.9 mV/$\sqrt{\text{Hz}}$ on a 5 μm × 5 μm pixel, corresponding to better than parts-per-hundred changes in redox molecule concentration down to nanomolar concentrations at 100-ms frame rates. This provides a new strategy for visualizing chemical reactions and biomolecules with a two-dimensional material screen.

INTRODUCTION

Transition metal dichalcogenides (TMDs) such as MoS_2 are two-dimensional (2D) semiconductors with a bandgap in the visible portion of the electromagnetic spectrum. TMDs have received great interest since the discovery that a monolayer of MoS_2 is a direct bandgap semiconductor with a reasonable photoluminescence (PL) efficiency (*1*, *2*). Since then, the PL of TMDs has been studied extensively and shown to respond to electrostatic gating (*3*, *4*), chemical doping (*5*, *6*), changes in pH (*7*), and defects (*8*, *9*). However, only a few studies have exploited this sensitivity to use MoS_2 PL as a chemical or biological sensor. Early work on biological sensors used ion intercalation schemes to optically measure cell viability (*10*, *11*). Researchers have also studied charge transfer processes between MoS_2 and a variety of electrolytes, observing charge transfer rates dependent on illumination intensity (*12*) and back-gate voltage (*13*).

One attractive application for TMDs, which has not been previously demonstrated, is the spatially resolved optical detection of redox

[1]Laboratory of Atomic and Solid State Physics, Cornell University, Ithaca, NY, USA. [2]Kavli Institute at Cornell for Nanoscale Science, Cornell University, Ithaca, NY, USA. [3]Department of Chemistry and Chemical Biology, Cornell University, Ithaca, NY, USA. [4]Department of Chemistry, Institute for Molecular Engineering, and James Franck Institute, University of Chicago, Chicago, IL, USA.
*These authors contributed equally to this work.
†Corresponding author. Email: plm23@cornell.edu

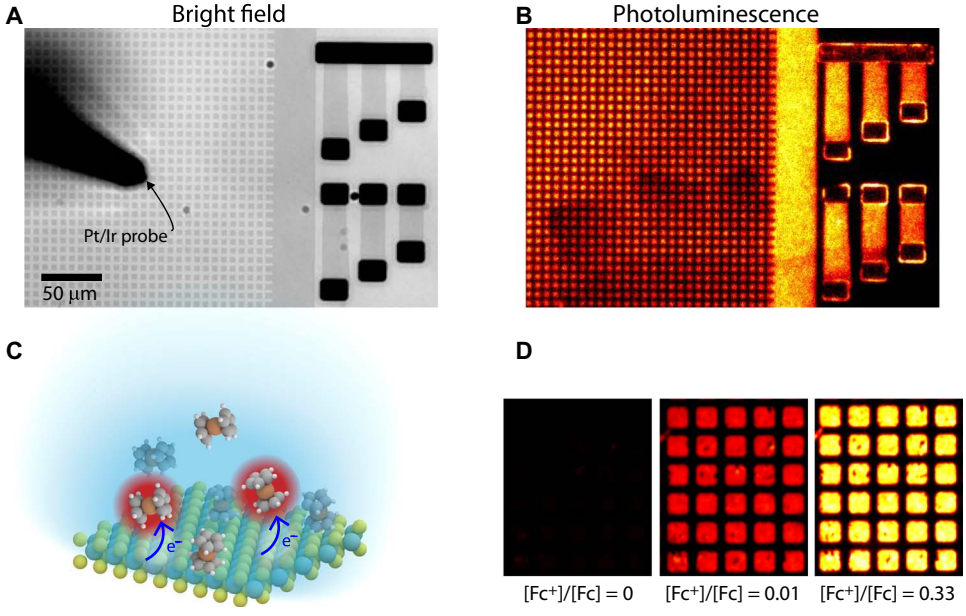

Fig. 1. MoS_2 PL response due to a change in $[Fc^+]/[Fc]$ ratio. (**A**) Bright-field transmitted light optical image of a MoS_2 pixel array consisting of 5 μm × 5 μm MoS_2 squares and Ti/Au contacted devices. The Pt/Ir electrode used to contact devices and oxidize the ferrocene molecules is shown in the middle of the image. (**B**) PL image of the same region in (A) excited by the 546-nm peak of a mercury lamp and imaged with a filter centered at 650 nm. The image shown is taken with a 2-s integration time. (**C**) Schematic of the charge transfer between ferrocene molecules and MoS_2. The red shade represents positively charged ferrocene molecules (ferrocenium). (**D**) PL of MoS_2 pixels varying the relative concentrations of ferrocene and ferrocenium.

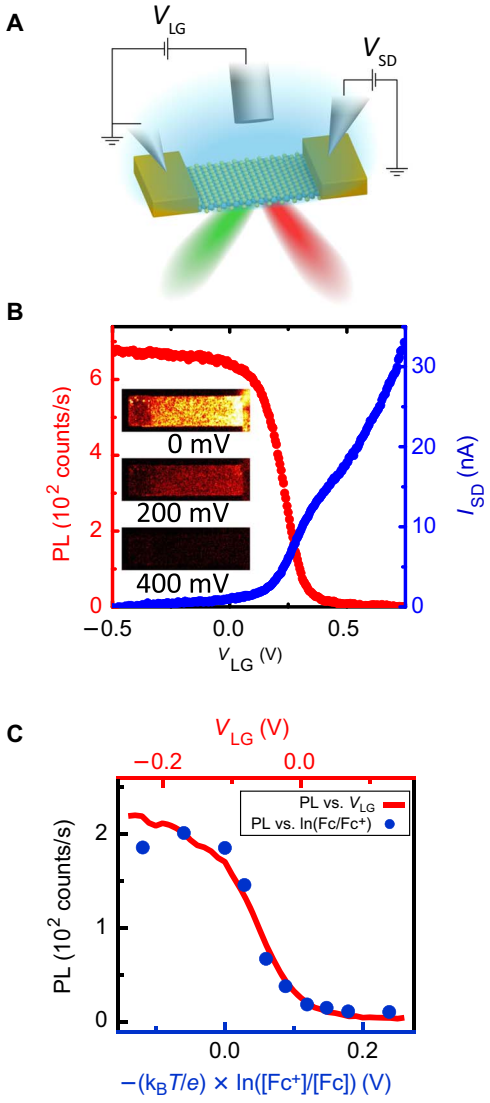

Fig. 2. MoS_2 PL response to ionic liquid gating. (**A**) Schematic and circuit diagram of the MoS_2 PL measurement as a function of the ionic liquid gate voltage (V_{LG}). (**B**) MoS_2 PL (red, left axis) and source-drain current (blue, right axis) as a function of the ionic liquid gate voltage for a solution of B_4NPF_6 (100 mM) in acetonitrile. Exposure time for images and data are 50 ms. (**C**) PL signal from gating of MoS_2 device and from MoS_2 pixels at different concentrations of ferrocene and ferrocenium. The correspondence between the two curves, using k_BT = 25.7 meV, indicates that sweeping the gate potential and changing the chemical potential cause an equivalent response for MoS_2. Data are taken with a 100-ms exposure time. Variation in the initial charge density of two different MoS_2 samples due to different surface adsorbates likely accounts for the difference in between the PL versus gate voltage curves (B) and (C).

molecules at the micrometer scale. Current approaches for spatially resolved redox molecule sensing include arrays of microelectrodes (*14*, *15*), altered complementary metal-oxide-semiconductor (CMOS) camera detectors (*16*), ion-sensitive field-effect transistor arrays (*17*), and scanning electrochemical microscopy (SECM) (*18*). These techniques, particularly microelectrode arrays and SECM, can be used for diverse applications and are unlikely to be completely replaced by any optical techniques. They demonstrate high-speed detection and resolution at the few micrometer level. However, in certain circumstances, a completely wireless readout of chemical activity and molecular concentration is advantageous. Existing optical detection methods include scanned photocurrent (*19*), porous silicon (*20*), and surface plasmon (*21*, *22*) techniques, and methods using fluorescent molecules and nanomaterials (*23*–*25*). Organic fluorescent molecules can be used to detect a wide variety of redox molecules with high spatial and temporal resolution but suffer from photobleaching (*24*, *25*), leading to interest in using photoluminescent nanomaterials in chemical sensing applications.

In this work, we show that MoS_2 pixel arrays are a powerful class of sensors for detecting redox-active molecules. Patterned arrays of MoS_2 squares are used to measure changes in redox concentrations with micrometer-scale spatial resolution and at 10-ms temporal resolution. We can detect concentration changes on the order of few nanomolar concentrations, on par with the best electrical microelectrode detectors. These MoS_2 pixels can be deployed in a wide variety of environments, from optical fibers to microfluidic systems, making them an attractive redox sensing platform for numerous applications.

RESULTS

The samples consist of photolithographically patterned MoS_2 directly grown on fused silica substrates using metal-organic chemical vapor deposition (*26*). We examine two different geometries: MoS_2 "pixel arrays" (Fig. 1A, left) consisting of small (2 μm × 2 μm or 5 μm × 5 μm) electrically floating squares, and MoS_2 ionic liquid gate transistors (Fig. 1A, right) with Ti/Au contacts. We patterned MoS_2 into pixels so that each pixel would be electrically isolated from all the others to measure the local chemical potential. For most of the measurements reported here, the samples were placed in a standard supporting electrolyte solution consisting of tetrabutylammonium hexafluorophosphate (Bu_4NPF_6) in acetonitrile. The redox couple ferrocene/ferrocenium was added as indicated. Similar results were obtained with other redox couples in aqueous environments. Details regarding the sample preparation process can be found in Materials and Methods and the Supplementary Materials.

Figure 1B shows the PL of MoS_2 in a solution of Bu_4NPF_6 in acetonitrile. Both the pixels and the devices show bright PL. The observed internal quantum efficiency of ~10^{-4} is comparable to others reported in the literature (*1*, *27*). Figure 1D shows the effect of the ferrocenium/ferrocene (Fc^+/Fc) redox couple on the PL intensity for different Fc^+/Fc ratios at a fixed 1 mM total concentration. The PL increases markedly with increasing concentration of ferrocenium. The Fc^+ ions serve to extract electrons from MoS_2, as shown schematically in Fig. 1C. This is consistent with the tuning of the PL in doped MoS_2 observed previously as a function of a solid-state back-gate voltage (*3*, *4*) and chemical doping with redox molecules (*6*). Additional increase of the PL could also occur due to defect screening by p-type molecules (*28*, *29*). The devices thus operate as redox sensors, with order-of-magnitude changes in PL seen when changing the Ox/Red ratio.

The doping of electrically floating MoS_2 pixels is akin to an open circuit potential (OCP) measurement. In an OCP measurement, the potential between a working electrode in solution and a reference electrode is measured in the absence of current flow, giving the electrochemical potential of the solution. In our case, changes in the PL of the MoS_2 pixels indicate a change in the chemical potential of the solution near the MoS_2 pixel, allowing spatially resolved chemical potentials to be optically read out. The mechanism can be understood by considering the

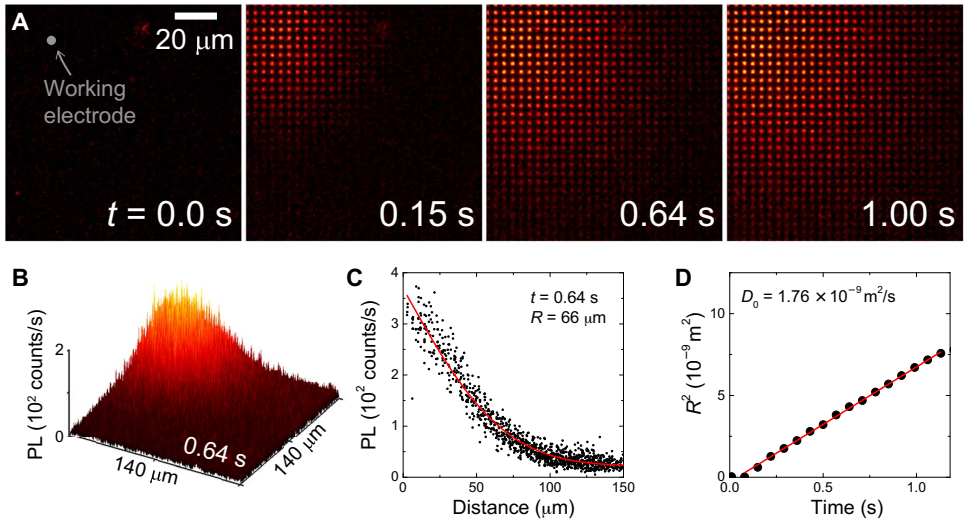

Fig. 3. Visualizing ferrocenium diffusion using a MoS_2 pixel array. (**A**) Time-lapse PL images of MoS_2 pixels (2 μm × 2 μm) after applying a 0.6-V square wave pulse to a working electrode (versus a distant large platinum electrode) located at the top left corner of the image at $t = 0$ s. The images show the MoS_2 pixels lighting up in response to the diffusion of ferrocenium ions. Exposure time for each image is 10 ms. (**B**) 3D surface plot of the image at 0.64 s, showing the spatial gradient of the PL signal. (**C**) Average PL value for each MoS_2 pixel in the image versus distance from the working electrode at $t = 0.64$ s. These data are fit with an error function centered at zero with characteristic length-scale $R = (4D_0t)^{0.5}$, where D_0 is the diffusion constant for ferrocenium. (**D**) Values for R^2 extracted from each frame versus time. Linear fitting of these data gives $D_0 = (1.76 \pm 0.02) \times 10^{-9}$ m^2/s, which matches well with other values found in the literature for ferrocenium.

chemical potential of the solution μ_s set by the ferrocene/ferrocenium ratio. This chemical potential is given by the Nernst equation

$$\mu_s = eE_0 + k_B T \ln\left(\frac{[Fc^+]}{[Fc]}\right) \quad (1)$$

where k_B is Boltzmann's constant, T is the temperature, and E_0 is the standard reduction potential. As described in the equation above, an increase in the ferrocenium/ferrocene ratio results in an increase in the liquid potential. This change in chemical potential is followed by the MoS_2 Fermi level due to charge transfer between MoS_2 and ferrocene/ferrocenium. Thus, the shift in the chemical potential acts as an effective gate voltage on MoS_2 that changes the electron density and therefore the PL. This sensing mechanism is not sensitive to a single redox species but gives a readout of the local chemical potential of the solution.

To demonstrate this quantitatively, we compare the response of the pixels to measurements of the gated devices, shown schematically in Fig. 2A. Figure 2B shows both the PL and the two-probe in-plane conductance of the MoS_2 transistors as a function of the ionic liquid voltage (V_{LG}). As seen in the figure, the PL of the device decreases with the addition of electrons ($V_{LG} > 0$), and simultaneously, the device begins to conduct. For $V_{LG} < 0$ V, the electrons are depleted and the PL increases and then saturates when the Fermi level of MoS_2 is in the bandgap of the semiconductor.

The equivalence of these different ways of shifting the charge density is demonstrated in Fig. 2C, where the PL of the pixels as a function of the chemical potential is plotted on the same graph as the dependence of the PL of the transistor devices on gate voltage. We observe a one-to-one correspondence between the change in liquid potential determined according to Eq. 1 and the directly applied ionic liquid gate voltage, with no rescaling. The two curves overlay accurately, indicating that the PL of the MoS_2 pixels is set by the shift in the chemical potential of the solution with changing redox molecule concentration. Measuring a gate curve before measuring PL of electrically floating MoS_2 as a function of redox molecule concentration thus allows us to interpolate between chemical potential and PL. While the data shown as red lines in Fig. 2 (B and C) are from gated devices, all of the rest of the data in this work are taken from MoS_2 pixels and pieces that are electrically floating.

Figure 3 shows the use of a pixel array to image a basic electrochemical process, the production of oxidized molecules at a working electrode. A microelectrode (position indicated in the first frame of Fig. 3A) is positioned 5 μm or less above the MoS_2 pixel array in a ferrocene solution with an initial ferrocene concentration $[Fc]_0 = 1$ mM. A voltage pulse is applied to the microelectrode going from a voltage below to above the oxidation voltage for ferrocene, $V_w = 0$ to 0.8 V. This fast voltage step results in the rapid oxidation of ferrocene to ferrocenium. A few milliseconds after the voltage pulse, we observe a large increase in the PL of the MoS_2 pixels around our electrode (Fig. 3A and movie S1, with a 3D plot showing the distribution of bright pixels shown in Fig. 3B). The cloud of Fc^+ diffuses outward from the microelectrode, lighting up the rest of the MoS_2 pixel array.

By following the size of the ferrocenium cloud as a function of time, we can directly measure its diffusion constant in the solution. For a localized source such as a microelectrode, the concentration of ferrocenium as a function of time (t) is expected to follow the form (*30*) $[Fc^+] = A \times \mathrm{erfc}\left(\frac{x}{\sqrt{4Dt}}\right)$, where erfc is the complementary error function, x is the distance from the microelectrode, and D is the diffusion constant of ferrocenium. By plotting pixel brightness as a function of x for each frame and fitting every plot with the above equation (Fig. 3C), we obtain the radius R of the ferrocenium cloud as a function of time. Figure 3D plots the square of this radius, which is predicted to grow linearly with time, $R^2 = 4Dt$ for simple diffusion. Linear fitting yields $D = (1.76 \pm 0.02) \times 10^{-9}$ m^2/s. This agrees with the values for

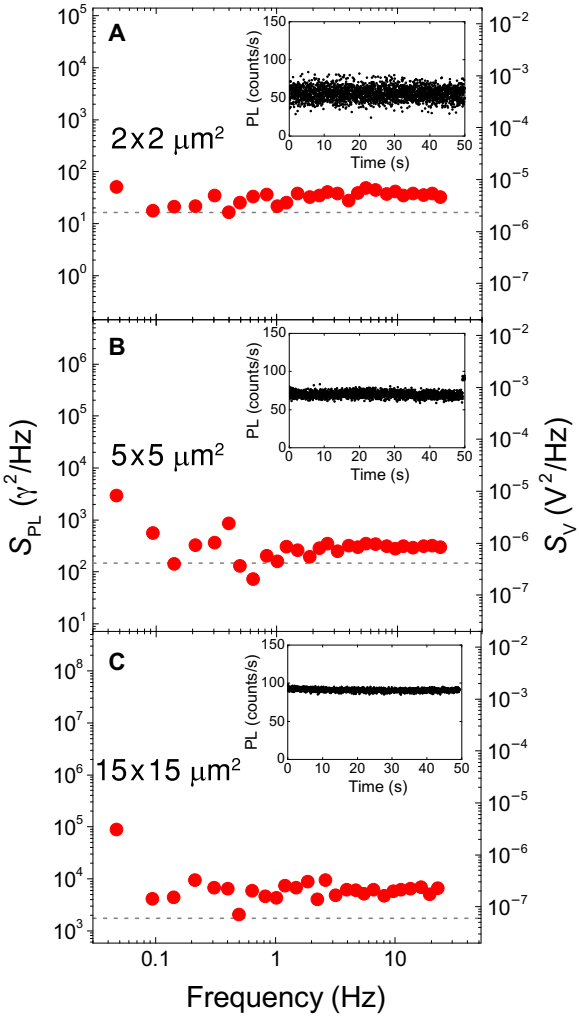

Fig. 4. MoS_2 pixel detector power spectral density. Noise power spectra of PL for three sizes of MoS_2 redox detectors. The left axis shows photons detected squared per hertz, and the right axis is converted to voltage via a MoS_2 gate curve. All curves are taken at 10-ms exposure times. Power spectrum for a 2 μm × 2 μm pixel (**A**), a 5 μm × 5 μm pixel (**B**), and a 15 μm × 15 μm MoS_2 region (**C**). The shot noise limit of our setup is shown by the dashed gray lines and corresponds to 1.5 mV/$\sqrt{\text{Hz}}$ for (A), 0.6 mV/$\sqrt{\text{Hz}}$ for (B), and 0.2 mV/$\sqrt{\text{Hz}}$ for (C). The insets show the PL versus time graphs from which the power spectra were calculated.

the diffusion constant of ferrocenium in acetonitrile found in the literature, 1.6×10^{-9} to 2.2×10^{-9} m^2/s (*31*). The ionic current can also be mapped by following the PL gradient as a function of time, showing a high ionic current near the microelectrode that decays rapidly as a function of the distance from the electrode (see fig. S4).

To determine the ultimate resolution of the pixel array to changes in redox concentrations, we examine noise properties of individual pixels. By recording the PL intensity of MoS_2 pixels as a function of time with 10-ms exposure times, shown in the insets of Fig. 4, we observe that the PL intensity fluctuates around a constant value at a constant concentration of ferrocene and ferrocenium. We study the noise in our devices for different MoS_2 areas: a 2 μm × 2 μm pixel (Fig. 4A), a 5 μm × 5 μm pixel (Fig. 4B), and a 15 μm × 15 μm region of a MoS_2 sheet (Fig. 4C). As expected, we observe that the signal-to-noise ratio increases with increasing area. The noise power spectra for all three regions are nearly frequency independent and lie close to the estimated shot noise from our experimental setup (shown by the dashed gray lines), which sets our ultimate noise floor. The noise level we detect is far greater than the read noise for our detector, which is reduced to subphoton levels by the electron-multiplying gain of the Andor iXon+ electron-multiplying charge-coupled device (EMCCD) camera. The shot noise in our setup arises from the finite number of photons reaching the camera and can be estimated by $\delta N = \sqrt{2N}$, where the factor of $\sqrt{2}$ accounts for added noise from the EMCCD gain of the camera. We also see small pixel-to-pixel variation in the intensity, which is less than 10% for 5 μm × 5 μm pixels (fig. S8).

This photon count noise can also be converted to a chemical potential noise by noting the equivalency between gate voltage and chemical potential shown in Fig. 2C. The count noise is turned into to a chemical potential noise by taking the derivative of the PL versus gate voltage curve at the average pixel brightness and using that derivative to convert between counts and voltage. The right axis in Fig. 4 shows the corresponding voltage noise density for the three regions with the panels plotted in the same scale for better comparison. We obtain a voltage noise density of 2 mV/$\sqrt{\text{Hz}}$ for the 2 μm × 2 μm MoS_2 pixel, 0.9 mV/$\sqrt{\text{Hz}}$ for the 5 μm × 5 μm MoS_2 pixel, and 0.5 mV/$\sqrt{\text{Hz}}$ for the 15 μm × 15 μm MoS_2 region. The voltage noise can be translated to an [Ox]/[Red] detection resolution through the Nernst equation. For a concentration ratio of ferrocenium to ferrocene ($r = [Fc^+]/[Fc]$), the resolution is given by $\delta r/r = d\mu/k_BT$. This gives a redox detection resolution of $\frac{\delta r}{r} = 0.03\ \text{Hz}^{-1/2}$ or 10% at a 25-Hz bandwidth on a 5 μm × 5 μm pixel. This detection limit, which is independent of the initial concentration, is advantageous for measuring changes in redox molecule concentration in dilute solutions, as we demonstrate below.

We now compare MoS_2 pixel redox sensors to the standard electrochemical method for measuring redox molecules, cyclic voltammetry (CV). We performed cyclic voltage sweeps at an ultramicroelectrode while monitoring the PL of nearby MoS_2, shown schematically in Fig. 5A. These measurements were done at ferrocene concentrations ranging from 50 μM to 1 mM, as seen in Fig. 5B. I_w abruptly increases when the working electrode voltage overcomes the oxidation voltage for ferrocene at roughly the same values for each concentration of ferrocene. Similarly, we observe a sharp increase in PL intensity above the ferrocene oxidation potential, coinciding with the turn on in current for the CV measurements. However, these two measurements have a crucial difference: While the current at the microelectrode scales linearly with the initial concentration, the PL produces roughly the same response to sweeps in voltage down to the micromolar range of initial concentrations of ferrocene (Fig. 5B). Because the PL response is not specific to ferrocene, the lowest concentration sweep at 50 μM is limited only by the background concentration of any other redox molecules in the solution. MoS_2 can be doped by any redox molecule that transfers charge with MoS_2. PL and CV curves for a system with ruthenocene and a mixture of ferrocene and ruthenocene can be seen in the Supplementary Materials (fig. S3). We observe that the PL responds to increases in concentration of both ferrocenium and ruthenocenium.

The CV measurements and MoS_2 PL measurements are related by the Nernst equation (Eq. 1). Assuming that the large initial ferrocene concentrations $[Fc]_0$ remains constant and the concentration of ferrocenium is proportional to the current to the working electrode (a valid assumption provided the electrochemical system is in steady state as defined in the Supplementary Materials), we can rewrite Eq. 1 as $\mu \propto k_BT \ln (I_W/[Fc]_0)$. Therefore, for the region of MoS_2 doping where the PL intensity is linear with the electrochemical potential, we expect

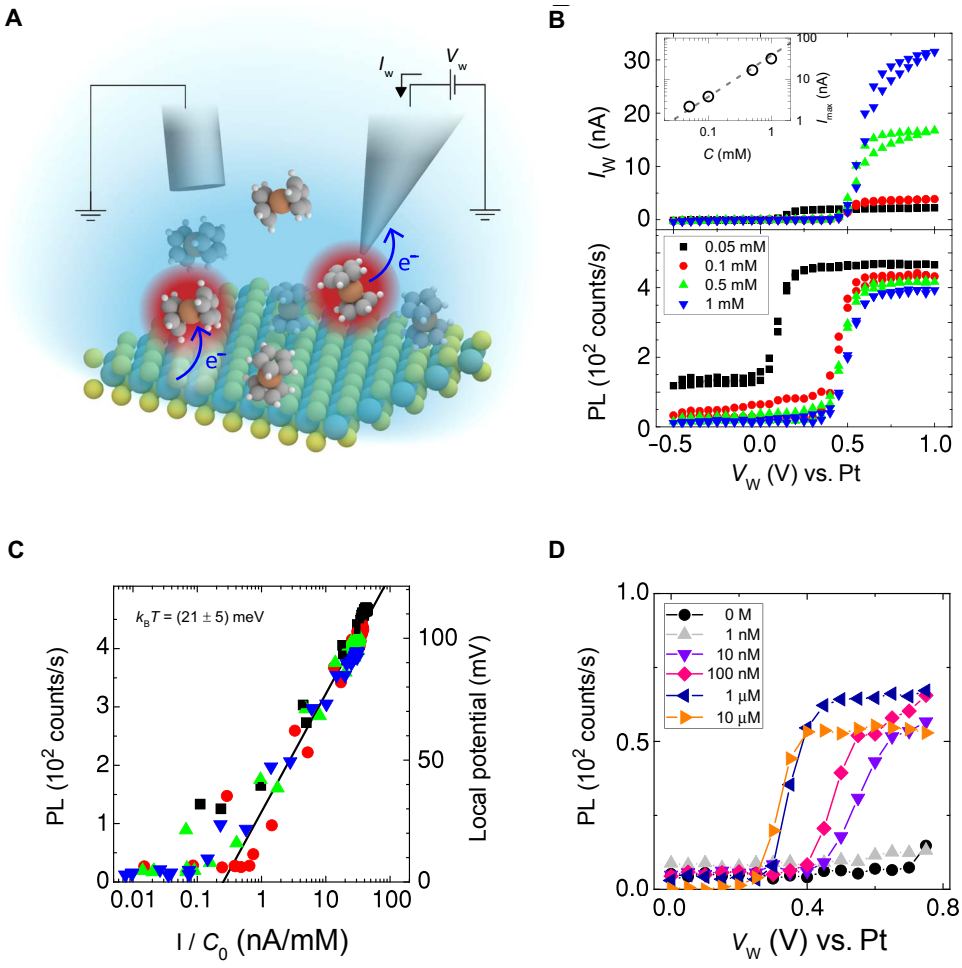

Fig. 5. MoS_2 PL for different ferrocene concentrations. (**A**) Schematic of CV experiment. The initial solution contains only ferrocene, which is oxidized to ferrocenium by applying a potential to a Pt/Ir microelectrode versus a large platinum wire far from the reaction site. The local change in concentration in ferrocenium dopes MoS_2, changing the brightness of the PL. (**B**) Top: Current (I_w) versus voltage (V_w) of the working electrode for different concentrations of ferrocene. Inset: Log-log plot of current at V_w = 1 V versus concentration of ferrocene. Bottom: MoS_2 PL versus working electrode voltage for different concentrations of ferrocene. Data are taken with 10-ms exposure time. (**C**) Effective change in potential on MoS_2 plotted against the working electrode current normalized by ferrocene concentration (C_0). The effective change in potential is obtained from the MoS_2 PL by using the slope of the linear region of the PL versus V_{LG} curve measured in the same device (inset). The experimental points collapse to one curve that is well described by the Nernst equation: $E = E' + (k_BT/e)\ln(I/C_0)$, with k_BT/e = (21 ± 5) mV and E' = (0.53 ± 0.01) V accounting for a current offset of −1 nA/mM. (**D**) PL versus electrode voltage for low concentrations of ferrocene. The first response is seen at 10 nM concentrations of ferrocene, likely limited by background concentrations of contaminant redox molecules. Data are taken with 100-ms exposure time.

that $\mathrm{PL} \propto k_B T \ln\left(\frac{I_W}{[Fc]_0}\right)$. By plotting this change in potential versus $\log\left(\frac{I_W}{[Fc]_0}\right)$, the data should collapse onto the same curve independent of ferrocene concentration. This is what we observe (Fig. 5C). Our data are well fit by Eq. 1 with k_BT/e = (21 ± 5) meV (with uncertainty in the conversion between PL and voltage constituting the largest source of error), indicating a simple relationship between standard current-based detection methods for calculating concentration and our method using MoS_2 PL.

Since the signal for MoS_2 PL detection of molecules is independent of absolute concentration and depends instead on the ratio of oxidized-to-reduced species, it provides a method for detecting redox molecules that scales favorably down to low concentrations. To test the detection limits of our system, we performed simultaneous CV sweeps and PL measurements of MoS_2 pixels at lower concentrations of ferrocene, shown in Fig. 5D. Although the current at our microelectrode falls below the detection limit of our setup for concentrations under 10 μM, the PL of MoS_2 attains the same value as a function of voltage for 10 and 1 μM concentrations. The response begins to shift at 100 and 10 nM concentrations, perhaps due to comparable concentrations of contaminant redox molecules, but still reaches the same peak PL intensity. The low detection limit of sub–10 nM concentrations using MoS_2 PL improves upon ultramicroelectrode detection limits for concentration detection, which are reported to be at best around 50 nM (*32*, *33*). The linear scaling of current at a microelectrode with concentration sets the detection limit for amperometric techniques. Assuming a microelectrode of the same area as our MoS_2 pixels (~100 μm^2) and linear scaling of the current with concentration, the current would be approximately 100 fA for a concentration of 10 nM.

Having explored the operation of the pixel arrays for redox sensing, we illustrate their use in a variety of situations. Figure 6 (A and B) shows a MoS_2 pixel array deployed in a polydimethylsiloxane (PDMS)

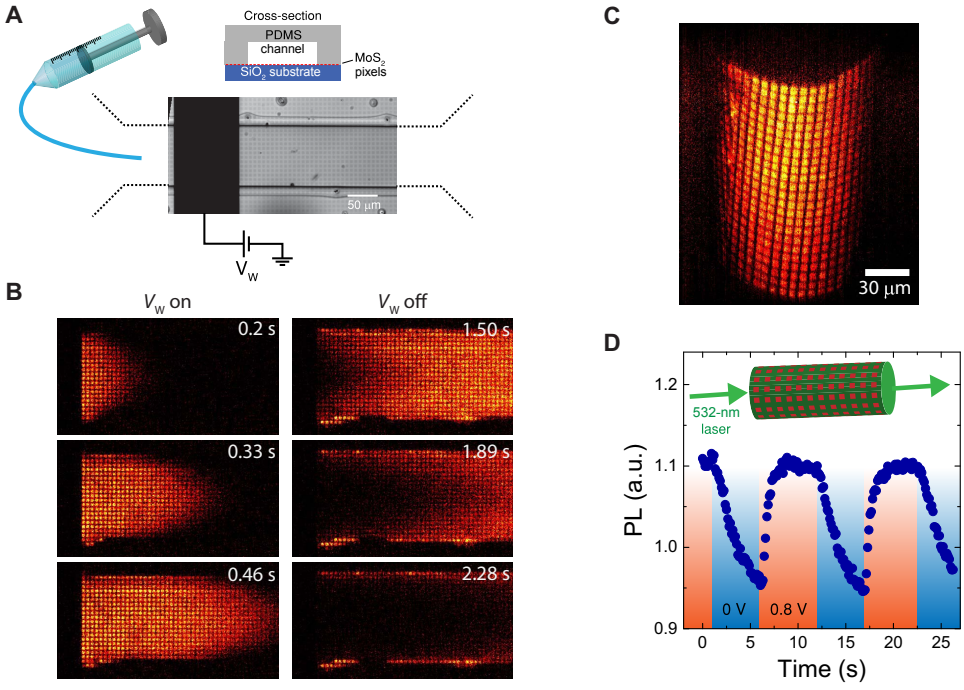

Fig. 6. Flow imaging in microfluidic channels with MoS_2 pixels and optical fiber. (**A**) Bright-field image of PDMS channel placed on substrate with MoS_2 pixel array and platinum surface electrode, with schematic showing circuit with voltage V_W for applying potentials to oxidize ferrocene and syringe for driving flow of solution. (**B**) PL images MoS_2 pixel array during laminar flow. A 1-V pulse is applied to the platinum surface electrode for 1 s to oxidize ferrocene. Images are taken with 100-ms exposure time. (**C**) Reconstructed confocal PL microscopy images showing MoS_2 pixels transferred onto an optical fiber. (**D**) Plot of chemical potential sensing with light coupled to MoS_2 through the optical fiber. As in previous experiments, a pulse is applied to a probe nearby MoS_2 to oxidize ferrocene to ferrocenium. MoS_2 is illuminated with a 532-nm laser coupled into the optical fiber, and the PL is observed with an optical microscope. Data are taken with 100-ms exposure time. a.u., arbitrary units.

microfluidic channel to measure the spatial distribution of the oxidation state of redox active molecules. A syringe pump connected to the channel supplies pressure-driven (laminar) flow, while a platinum surface electrode on chip can be used to perform redox chemistry in the channel. A short pulse applied to the surface electrode oxidizes ferrocene in the channel to ferrocenium, which is carried to the right by the flow. The resultant PL response of the MoS_2 pixel array is shown in Fig. 6B and movie S2, allowing the direct tracking of the oxidized molecules in real time with micrometer and millisecond spatial and temporal resolution. Similar results for electroosmotic flow are shown in the Supplementary Materials.

These pixel arrays can be transferred to almost any substrate. Figure 6C shows a MoS_2 pixel array on an optical fiber where the light through the fiber is used to excite the pixels. Figure 6D shows a measurement of the PL, as a probe nearby periodically oxidizes ferrocenium.

DISCUSSION

This work demonstrates a previously unknown class of 2D fluorescent sensors for the detection of redox-active species. The sensor is shot noise limited, with a sensitivity of 10% in a 30-Hz bandwidth at a 5 μm × 5 μm pixel and detection limits down to nanomolar concentrations. Improvements to the PL efficiency could increase this sensitivity by another one to two orders of magnitude. Future work could also include functionalization of MoS_2 for specific molecular detection, following approaches used for other photoluminescent nanomaterials (*23*, *34*, *35*). The fast, all-optical detection of chemical potentials and ionic densities using the PL of a 2D material has great potential for monitoring various chemical and biological systems, such as hydrogen evolution reactions and neurological activity (the Supplementary Materials present initial measurements of dopamine). Being flexible, chemical inert, and easily transferrable, MoS_2 provides a local redox sensing method that can be easily incorporated into a broad range of environments and systems.

MATERIALS AND METHODS

MoS_2 growth and device fabrication

The MoS_2 sheets were grown by metal-organic chemical vapor deposition on 1″ fused silica wafers as described in (*26*). After initial PL and atomic force microscopy characterizations (fig. S1), we defined Ti/Au (5/50 nm) electrodes and alignment markers using conventional optical lithography and metal evaporation methods. The MoS_2 structures (pixels and device channels) were defined by a final optical lithography step followed by reactive ion etching (SF_6:O_2 5:1 ratio at 20 W). To increase the PL quantum efficiency in our films, we treated our final structures with bis(trifluoromethane) sulfonimide following the procedures detailed in (*27*).

Experimental setup

The devices were measured using a probe station with automated micromanipulators (Sensapex). The samples were mounted with the MoS_2 side pointing up on an inverted microscope and imaged with a water immersion 60× objective with numerical aperture 1.25 and an Andor EMCCD.

The PL measurements were made using a mercury arc lamp combined with a 550-nm band-pass filter [40-nm full width at half maximum (FWHM), Thorlabs] and a dichroic mirror (552-nm

long pass, Semrock) as our incident light beam. The reflected light is partially filtered by the dichroic beamsplitter and further selected using a 650-nm band-pass filter (40-nm FWHM, Thorlabs), which includes the *A*-exciton peak at room temperature (~660 nm). For the electrochemical measurements, we used a Pt wire as our quasi-reference electrode and Pt/Ir microelectrode probes (Microprobes for Life Sciences) with ~1 megaohm impedance at 1 kHz to the liquid as our working electrode.

Electrolyte and ferrocene solution preparation

The electrolyte solution for all the measurements presented consisted of 100 mM Bu_4NPF_6 (Sigma-Aldrich) in acetonitrile. After the electrolyte preparation, the desired amount of ferrocene (Sigma-Aldrich) was mixed to obtain the concentrations ranging from 1 nM to 100 mM used in our work.

The desired solution was then pipetted onto the fused silica chips containing the MoS_2 structures, which sat on an inverted microscope. The liquid was contained by a PDMS ring (~2 mm thick), which sealed onto the wafer. For the measurements with increasing ferrocene concentration, we started with the lowest concentration and increased it by pipetting away the lower concentration and flushing the liquid with the higher concentration solution. If a series of measurements were required, the samples were flushed in acetonitrile several times to remove any adsorbed ferrocene molecules.

SUPPLEMENTARY MATERIALS

Supplementary material for this article is available at http://advances.sciencemag.org/cgi/content/full/5/11/eaat9476/DC1

Supplementary Materials and Methods

Fig. S1. Characterization of MoS_2 samples.

Fig. S2. Diagram of the experimental setup.

Fig. S3. Detection of ions in solutions containing ruthenocene and ruthenocene/ferrocene mixtures.

Fig. S4. Diffusion current mapping of ferrocene ions.

Fig. S5. PL decay time for varied Fc concentrations.

Fig. S6. PL imaging of electroosmotic flow.

Fig. S7. PL versus dopamine concentration.

Fig. S8. Pixel-to-pixel variation of PL.

Movie S1. Visualizing ferrocenium diffusion using a MoS_2 pixel array.

Movie S2. Visualizing laminar flow of ions in a microfluidic channel.

Movie S3. Visualizing electroosmotic flow of ions in a microfluidic channel.

REFERENCES AND NOTES

1. K. F. Mak, C. Lee, J. Hone, J. Shan, T. F. Heinz, Atomically ThinMoS2: A new direct-gap semiconductor. *Phys. Rev. Lett.* **105**, 136805 (2010).
2. A. Splendiani, L. Sun, Y. Zhang, T. Li, J. Kim, C. Y. Chim, G. Galli, F. Wang, Emerging photoluminescence in monolayer MoS_2. *Nano Lett.* **10**, 1271–1275 (2010).
3. K. F. Mak, K. He, C. Lee, G. H. Lee, J. Hone, T. F. Heinz, J. Shan, Tightly bound trions in monolayer MoS_2. *Nat. Mater.* **12**, 207–211 (2013).
4. A. K. M. Newaz, D. Prasai, J. I. Ziegler, D. Caudel, S. Robinson, R. F. Haglund Jr., K. I. Bolotin, Electrical control of optical properties of monolayer MoS_2. *Solid State Commun.* **155**, 49–52 (2013).
5. N. Peimyoo, W. Yang, J. Shang, X. Shen, Y. Wang, T. Yu, Chemically driven tunable light emission of charged and neutral excitons in monolayer WS_2. *ACS Nano* **8**, 11320–11329 (2014).
6. S. Mouri, Y. Miyauchi, K. Matsuda, Tunable photoluminescence of monolayer MoS_2 via chemical doping. *Nano Lett.* **13**, 5944–5948 (2013).
7. W. Zhang, K. Matsuda, Y. Miyauchi, pH-dependent photoluminescence properties of monolayer transition-metal dichalcogenides immersed in an aqueous solution. *J. Phys. Chem. C* **122**, 13175–13181 (2018).
8. H. Nan, Z. Wang, W. Wang, Z. Liang, Y. Lu, Q. Chen, D. He, P. Tan, F. Miao, X. Wang, J. Wang, Z. Ni, Strong photoluminescence enhancement of MoS_2 through defect engineering and oxygen bonding. *ACS Nano* **8**, 5738–5745 (2014).
9. N. Kang, H. P. Paudel, M. N. Leuenberger, L. Tetard, S. I. Khondaker, Photoluminescence quenching in single-layer MoS_2 via oxygen plasma treatment. *J. Phys. Chem. C* **118**, 21258–21263 (2014).
10. Y. Wang, J. Z. Ou, S. Balendhran, A. F. Chrimes, M. Mortazavi, D. D. Yao, M. R. Field, K. Latham, V. Bansal, J. R. Friend, S. Zhuiykov, N. V. Medhekar, M. S. Strano, K. Kalantar-zadeh, Electrochemical control of photoluminescence in two-dimensional MoS_2 nanoflakes. *ACS Nano* **7**, 10083–10093 (2013).
11. J. Z. Ou, A. F. Chrimes, Y. Wang, S. Y. Tang, M. S. Strano, K. Kalantar-zadeh, Ion-driven photoluminescence modulation of quasi-two-dimensional MoS_2 nanoflakes for applications in biological systems. *Nano Lett.* **14**, 857–863 (2014).
12. M. Velický, M. A. Bissett, C. R. Woods, P. S. Toth, T. Georgiou, I. A. Kinloch, K. S. Novoselov, R. A. W. Dryfe, Photoelectrochemistry of pristine mono- and few-layer MoS_2. *Nano Lett.* **16**, 2023–2032 (2016).
13. Y. Wang, C.-H. Kim, Y. Yoo, J. E. Johns, C. D. Frisbie, Field effect modulation of heterogeneous charge transfer kinetics at back-gated two-dimensional MoS_2 electrodes. *Nano Lett.* **17**, 7586–7592 (2017).
14. J. Wang, R. Trouillon, Y. Lin, M. I. Svensson, A. G. Ewing, Individually addressable thin-film ultramicroelectrode array for spatial measurements of single vesicle release. *Anal. Chem.* **85**, 5600–5608 (2013).
15. I. Hafez, K. Kisler, K. Berberian, G. Dernick, V. Valero, M. G. Yong, H. G. Craighead, M. Lindau, Electrochemical imaging of fusion pore openings by electrochemical detector arrays. *Proc. Natl. Acad. Sci. U.S.A.* **102**, 13879–13884 (2005).
16. D. L. Bellin, H. Sakhtah, Y. Zhang, A. Price-Whelan, L. E. P. Dietrich, K. L. Shepard, Electrochemical camera chip for simultaneous imaging of multiple metabolites in biofilms. *Nat. Commun.* **7**, 10535 (2016).
17. P. Shields, B. Nemeth, R. B. Green, M. O. Riehle, D. R. S. Cumming, High-speed imaging of 2-D ionic diffusion using a 16 × 16 pixel CMOS ISFET array on the microfluidic scale. *IEEE Sens. J.* **12**, 2744–2749 (2012).
18. A. J. Bard, F. R. Fan, D. T. Pierce, P. R. Unwin, D. O. Wipf, F. Zhou, Chemical imaging of surfaces with the scanning electrochemical microscope. *Science* **254**, 68–74 (1991).
19. D. G. Hafeman, J. W. Parce, H. M. McConnell, Light-addressable potentiometric sensor for biochemical *systems. Science* **240**, 1182–1185 (1988).
20. A. Jane, R. Dronov, A. Hodges, N. H. Voelcker, Porous silicon biosensors on the advance. *Trends Biotechnol.* **27**, 230–239 (2009).
21. X. Shan, U. Patel, S. Wang, R. Iglesias, N. Tao, Imaging local electrochemical current via surface plasmon resonance. *Science* **327**, 1363–1366 (2010).
22. K. M. Mayer, J. H. Hafner, Localized surface plasmon resonance sensors. *Chem. Rev.* **111**, 3828–3857 (2011).
23. E. Polo, S. Kruss, Nanosensors for neurotransmitters. *Anal. Bioanal. Chem.* **408**, 2727–2741 (2016).
24. Z. Lou, P. Li, K. Han, Redox-responsive fluorescent probes with different design strategies. *Acc. Chem. Res.* **48**, 1358–1368 (2015).
25. E. H. Kim, G. Chin, G. Rong, K. E. Poskanzer, H. A. Clark, Optical probes for neurobiological sensing and imaging. *Acc. Chem. Res.* **51**, 1023–1032 (2018).
26. K. Kang, S. Xie, L. Huang, Y. Han, P. Y. Huang, K. F. Mak, C. J. Kim, D. Muller, J. Park, High-mobility three-atom-thick semiconducting films with wafer-scale homogeneity. *Nature* **520**, 656–660 (2015).
27. M. Amani, R. A. Burke, X. Ji, P. Zhao, D. H. Lien, P. Taheri, G. H. Ahn, D. Kirya, J. W. Ager III, E. Yablonovitch, J. Kong, M. Dubey, A. Javey, High luminescence efficiency in MoS_2 grown by chemical vapor deposition. *ACS Nano* **10**, 6535–6541 (2016).
28. W. Su, H. Dou, D. Huo, N. Dai, L. Yang, Enhancing photoluminescence of trion in single-layer MoS_2 using *p*-type aromatic molecules. *Chem. Phys. Lett.* **635**, 40–44 (2015).
29. W. Su, H. Dou, J. Li, D. Huo, N. Dai, L. Yang, Tuning photoluminescence of single-layer MoS_2 using H_2O_2. *RSC Adv.* **5**, 82924–82929 (2015).
30. A. J. Bard, L. R. Faulkner, *Electrochemical Methods: Fundamentals and Applications* (Wiley, 2000).
31. Y. Wang, E. I. Rogers, R. G. Compton, The measurement of the diffusion coefficients of ferrocene and ferrocenium and their temperature dependence in acetonitrile using double potential step microdisk electrode chronoamperometry. *J. Electroanal. Chem.* **648**, 15–19 (2010).
32. I. F. Cheng, L. D. Whiteley, C. R. Martin, Ultramicroelectrode ensembles. Comparison of experimental and theoretical responses and evaluation of electroanalytical detection limits. *Anal. Chem.* **61**, 762–766 (1989).
33. P. Hernández, I. Sánchez, F. Patón, L. Hernández, Cyclic voltammetry determination of epinephrine with a carbon fiber ultramicroelectrode. *Talanta* **46**, 985–991 (1998).
34. R. Freeman, I. Willner, Optical molecular sensing with semiconductor quantum dots (QDs). *Chem. Soc. Rev.* **41**, 4067–4085 (2012).
35. A. A. Boghossian, J. Zhang, P. W. Barone, N. F. Reuel, J. H. Kim, D. A. Heller, J. H. Ahn, A. J. Hilmer, A. Rwei, J. R. Arkalgud, C. T. Zhang, M. S. Strano, Near-infrared fluorescent sensors based on single-walled carbon nanotubes for life sciences applications. *ChemSusChem* **4**, 848–863 (2011).

Acknowledgments: We thank H. Abruña, M. Velicky, M. Lee, and W.R. Browne for fruitful discussions, and M. Ramaswamy for helping with the confocal PL imaging. **Funding:** This work was supported by the Cornell Center for Materials Research with funding from the NSF MRSEC program (DMR-1719875), by the Air Force Office of Scientific Research (MURI: FA9550-16-1-0031), and by the Kavli Institute at Cornell for Nanoscale Science. Additional funding was provided by the Samsung Advanced Institute of Technology and the University of Chicago MRSEC (NSF DMR-1420709). M.H.D.G. acknowledges funding from the Kavli Institute at Cornell and the Netherlands Organization for Scientific Research (NWO Rubicon 680-50-1311). This work made use of the NSF-supported Cornell Nanoscale Facility (ECCS-1542081) and the Cornell Center for Materials Research Shared Facilities, which are supported through the NSF MRSEC Program (DMR-1719875). **Author contributions:** M.F.R., M.H.D.G., J.P., and P.L.M. conceived the experiments. H.G. and K.K. performed the growth of the MoS_2 films under the supervision of J.P. M.F.R. and M.H.D.G. fabricated the samples and performed the experiments with assistance from A.J.C. and under the supervision of P.L.M., J.P., and D.C.R. M.F.R., M.H.D.G., and P.L.M. performed the data analysis and wrote the manuscript with comments from all authors. **Competing interests:** The authors declare that they have no competing interests. **Data and materials availability:** All data needed to evaluate the conclusions in the paper are present in the paper and/or the Supplementary Materials. Additional data related to this paper may be requested from the authors.

Submitted 12 September 2018
Accepted 17 September 2019
Published 8 November 2019
10.1126/sciadv.aat9476

Citation: M. F. Reynolds, M. H. D. Guimarães, H. Gao, K. Kang, A. J. Cortese, D. C. Ralph, J. Park, P. L. McEuen, MoS_2 pixel arrays for real-time photoluminescence imaging of redox molecules. *Sci. Adv.* **5**, eaat9476 (2019).

MoS_2 pixel arrays for real-time photoluminescence imaging of redox molecules

M. F. Reynolds, M. H. D. Guimarães, H. Gao, K. Kang, A. J. Cortese, D. C. Ralph, J. Park and P. L. McEuen

Sci Adv **5** (11), eaat9476.
DOI: 10.1126/sciadv.aat9476